



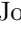





Electron coherent phonon coupling in $\text{Pr}_{0.5}\text{Ca}_{1.5}\text{MnO}_4$ measured with ultrafast broadband spectroscopy

Emmanuel B. Amuah ^{1,2} Khalid M. Siddiqui ^{2,*} Maurizio Monti ² Daniel Pérez-Salinas ^{2,3} Hanna Strojcka ^{2,4} Thomas H. Meyland ² Allan S. Johnson ⁵ and Simon E. Wall ^{2,†}

¹*ICFO - Institut de Ciències Fotòniques, The Barcelona Institute of Science and Technology, Av. Carl Friedrich Gauss 3, 08860 Castelldefels, Barcelona, Spain*

²*Department of Physics and Astronomy, Aarhus University, Ny Munkegade 120, 8000 Aarhus C, Denmark.*

³*ALBA Synchrotron Light Source, Cerdanyola del Valles, 08290 Barcelona, Spain*

⁴*Univ Rennes, CNRS, Institut de Physique de Rennes – UMR 6251, 35000 Rennes, France.*

⁵*IMDEA Nanoscience, Madrid, Spain.*

(Dated: August 21, 2025)

Photoexcitation of single-layered $\text{La}_{0.5}\text{Sr}_{1.5}\text{MnO}_4$ has played a key role in understanding orbital ordering and non-thermal states in the manganites. However, while orbital ordering in $\text{La}_{0.5}\text{Sr}_{1.5}\text{MnO}_4$ breaks the in-plane C_4 symmetry, many layered manganites show much more complex phase diagrams in which orbital ordering emerges from an already symmetry-broken high-temperature phase and also exhibit additional low-temperature phases. In this work, we examine the role of these phases in relation to orbital ordering in the single-layered manganite $\text{Pr}_{0.5}\text{Ca}_{1.5}\text{MnO}_4$ with a combination of optical reflection anisotropy and ultrafast broadband pump-probe spectroscopy. We find that the reflection anisotropy, measured in equilibrium, is strongly sensitive to charge and orbital-ordering transition only. However, the ultrafast response, measuring the non-equilibrium state is sensitive to all phases. In particular, we deduce that coherent phonons modulate unoccupied electronic states that are sensitive to the different phases of the material. This gives rise to a non-linear scaling of the phonon signal with pump fluence at specific probe wavelengths.

I. INTRODUCTION

Structural and electronic ordering are ubiquitous in strongly correlated materials, often leading to broken symmetries, and give rise to diverse and emergent functionalities [1–3]. Understanding how these ordering phenomena manifest is key to controlling the complex behaviors of correlated systems. To this end, mixed-valence manganites have provided a fertile platform for studying the strong competition between electronic, structural, orbital, and spin degrees of freedom that govern material properties [4, 5], hosting different long-ranged ordered states of charges, spin and orbitals. The three-dimensional $\text{A}_{1-x}\text{A}'_x\text{MnO}_3$ compounds have been studied in great detail due to their rich variety of ordered phases, colossal magnetoresistance effects [6–8], and light-induced phase transitions [9–15].

The single-layered manganites, $\text{A}_{1-x}\text{A}'_x\text{MnO}_4$, are less studied because the colossal magnetoresistance effect is suppressed in comparison to their three-dimensional counterparts [16], but are often regarded as model systems because the layered structure means that the physics of interest is confined to the two-dimensional manganese oxide planes. And, while $\text{La}_{0.5}\text{Sr}_{1.5}\text{MnO}_4$ (LSMO) has played a critical role in understanding orbital ordering [17–19] and its dynamics following optical [20–24], mid-IR [25, 26] and THz

excitation [27], other single-layered compounds have received less attention, particularly when driven out-of-equilibrium. Yet, many layered manganites show much richer phase diagrams and more complex structural changes than LSMO, which could help elucidate the roles of lattice and electronic correlations in determining the material properties. $\text{Pr}_{0.5}\text{Ca}_{1.5}\text{MnO}_4$ (PCMO) is such a material.

Orbital ordering in LSMO emerges from a tetragonal ($I4/mmm$) phase on cooling below $T_c \sim 220$ K and below $T_N = 110$ K antiferromagnetic order sets in. However, PCMO has a much richer phase diagram. The current understanding of the crystal structure of PCMO comes from a combination of electron diffraction and X-ray diffraction (XRD) studies [28–31], with the proposed structures depicted in Fig. 1. Like LSMO, at high temperatures, PCMO is in a high-temperature tetragonal phase (HTT) with the space group $I4/mmm$. However, already below $T_{LTO} = 466$ K, the system enters a low-temperature orthorhombic phase (LTO) due to an out-of-plane rotation of the oxygen octahedra that breaks the in-plane C_4 symmetry. In addition, strain develops along the b axis resulting in an orthorhombic unit cell represented by the $Bmcb$ space group. At $T_{\text{COO}} \sim 320$ K, the system undergoes a charge and orbital ordering (COO) transition, accompanied by a significant increase in resistivity and enhanced in-plane symmetry breaking concomitant with Jahn-Teller distortion of crystal. Within this phase, the charges form a checkerboard pattern, often represented with alternating Mn^{3+} and Mn^{4+} sites, although the actual charge disproportionation, δ , is typically very small. This transition doubles the length

* khalid.siddiqui@phys.au.dk

† simon.wall@phys.au.dk

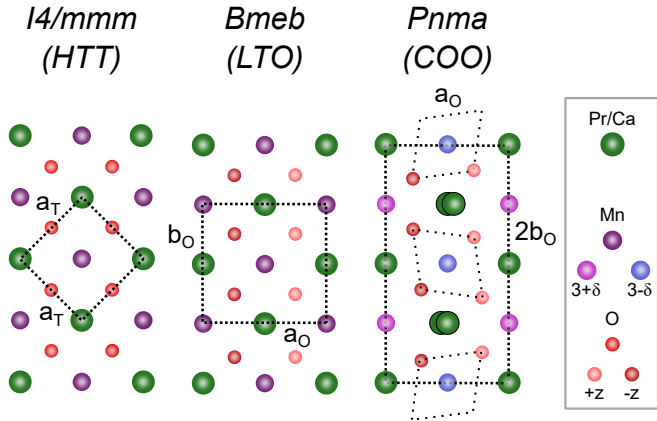


FIG. 1. Proposed structures across different phases of $\text{Pr}_{0.5}\text{Ca}_{1.5}\text{MnO}_4$ in the ab plane. In the $Bmcb$ phase the oxygen ions rotate around the a axis resulting in a displacement along the out-of-plane z -direction. In the $Pnma$ phase, the Jahn-Teller distortion doubles the periodicity along the b axis resulting in the Mn ion being situated in two inequivalent positions, which results in a small charge disproportionation, δ . HTT: High-temperature tetragonal; LTO: Low-temperature orthorhombic; COO: charge and orbital ordering.

of the b axis and the structure is characterized by the $Pnma$ space group, although some ambiguity remains about this assignment [29]. At lower temperatures, further structural transitions occur and at $T^* = 146$ K, the system moves into a low-temperature less orthorhombic (LTLO) phase where the difference between the a_O and b_O lengths shrinks [30], which is believed to arise from a change in the oxygen tilting scheme. Finally, 3D antiferromagnetism sets in at $T_N = 130$ K, with two-dimensional magnetic fluctuations possibly extending up to 200 K [32].

The ultrafast structural response to optical excitation in PCMO was previously studied by Porer *et al.* using time-resolved XRD at 100 K, where the amplitude of the Bragg peak associated with COO was tracked as the order parameter [30]. The COO phase was found to melt in less than 100 fs and the strong role of lattice was reported by the authors. Although, the time resolution did not allow to resolve the Jahn-Teller mode [10, 33–35], the melting and recovery of the COO phase was suggested to be tightly coupled to it, thus demonstrating the key connection between structural degree of freedom and long-range order. However, being a structural probe, direct information about the electronic changes was not available which motivates further investigation of the interplay of the electronic order with other degrees of freedom following optical excitation on ultrafast timescales, also in other phases of PCMO.

Here, we examine the optical and ultrafast response of PCMO using a combination of angle-resolved birefringence measurements and ultrafast broadband spectroscopy. Our work reveals the existence of local order in the LTO phase of PCMO and a pronounced rotation

of the optical axis upon entering the COO phase. The latter observation is at odds with the currently assigned space group. Moreover, the ultrafast response across different phases reveals intriguing trends, and analysis of the coherent phonon response presented here uncovers a breakdown in the linear relationship between the induced phonon displacement and the measured changes in reflectivity at specific probe wavelengths. Altogether, these observations showcase the complex and rich nature of the ultrafast response in PCMO.

II. METHODS

Single crystalline samples of PCMO were grown by floating zone technique, polished to give a (001) surface normal and mounted in an optical cryostat. Temperature-dependent optical anisotropy measurements were performed using the setup described in Ref. [36] with a probe wavelength of 1300 nm. High time-resolution pump-probe experiments were performed with 1.8 μm pump and visible probe as described in Ref. [37]. Pump and probe polarizations were parallel and along a/b axis. The probe pulse was dispersed inside a home-built spectrometer and detected by a CCD array on a shot-to-shot basis. The repetition rates were set at 1 kHz (probe) and 500 Hz (pump), and the differential reflectivity as a function of probe wavelength was calculated as the difference between the pumped and unpumped reflectivity at each time delay, $\frac{\Delta R}{R}(\lambda, t)$. The raw data is available in Ref. [38].

III. RESULTS AND DISCUSSIONS

A. Optical anisotropy

We start by examining the temperature-dependent reflection anisotropy to characterize the structural phase transitions in PCMO. Figure 2a shows the polarization-dependent reflectivity of PCMO in the charge/orbital phase (blue, $T = 200$ K) as well as at (orange, $T = 325$), and above (blue, $T = 360$ K) the COO phase transition temperature, represented in polar form. Anisotropy is observed at all three temperatures reflecting the fact that, unlike LSMO, PCMO remains orthorhombic above T_{COO} . The LTO phase shows only a weak anisotropy despite the orthorhombic structure, but the anisotropy becomes significantly larger when the system enters the charge/orbital ordering phase. Curiously, we observe that the optical axis also rotates significantly between the two phases.

Figure 2b shows the extracted angle which the optical axis makes relative to the crystallographic axis as a function of temperature. On cooling towards T_{COO} , the pattern rotates by several degrees before jumping at $T_{\text{COO}} \sim 325$ K. Although not shown here, the optical anisotropy showed no further changes when cooled below

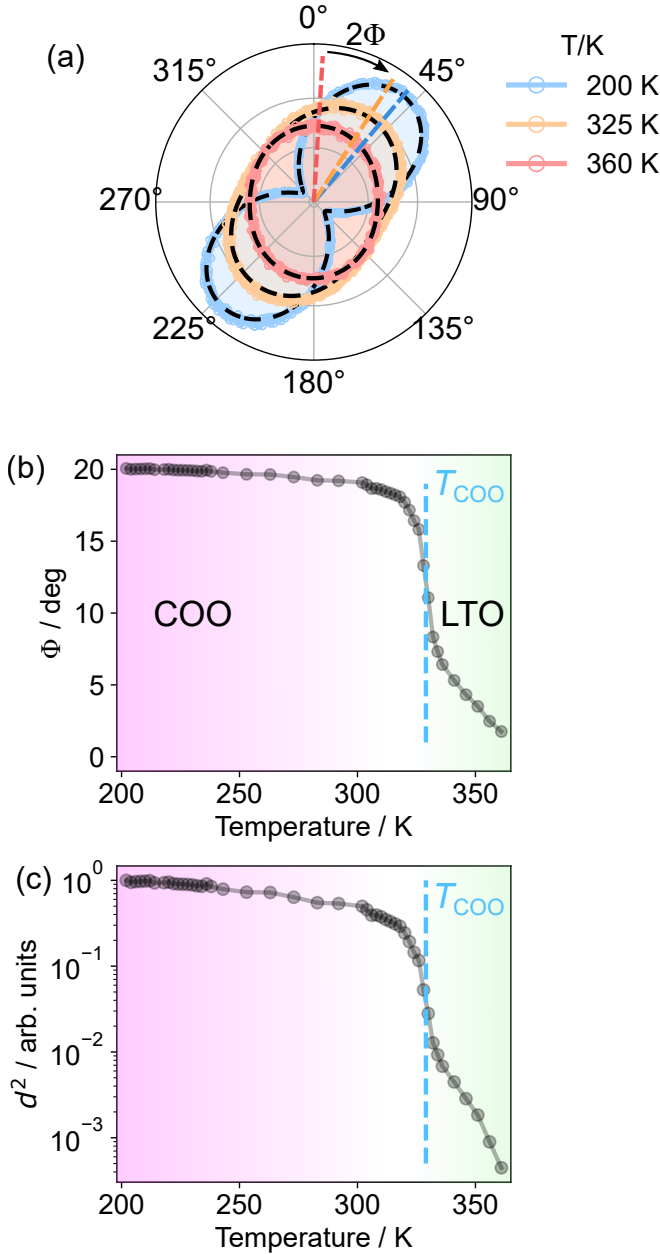


FIG. 2. (a) Polarization-resolved reflectivity patterns of $\text{Pr}_{0.5}\text{Ca}_{1.5}\text{MnO}_4$ at three temperatures. The *Bmcb* phase at $T = 200$ K (blue) in the charge/orbital ordered, at the phase transition temperature $T = 325$ K (orange), and in the LTO phase at $T = 360$ K (red). Markers are measurements and black dashed lines are fits to the data using the model described in the main text. $\Phi = 0$ corresponds to the probe light along the a crystallographic axis in the *Bmcb* phase. Colored dashed lines indicate the orientation of the optical axis relative to the crystallographic axis. (b) Temperature-dependent rotation of the optical axis as a function of temperature. System rotates its optical axis upon cooling towards the COO phase after which a step-like change is observed at the T_{COO} . The change saturates below this temperature. Blue dashed vertical line marks the transition temperature, T_{COO} and the shading separates COO phase from LTO. (c) Extracted order parameter d^2 as a function of temperature on a semi-log scale. Above T_{COO} , a small anisotropy of B_{1g} symmetry is still present, but 10^{-2} – 10^{-3} times weaker than in the ordered phase potentially indicating some short range order persists above T_{COO} .

T^* . This is surprising given that the system becomes less orthorhombic in LTLO phase, which may be expected to reduce the birefringent signal. This could be related to formation of a multi-domain state, with domains smaller than the probe spot size, or points to the fact that the charge/orbital ordering is by far the strongest perturbation to the electronic structure at this probed wavelength, consistent with recent experiments on thin film samples which have shown that charge/orbital ordering is insensitive to the small oxygen rotations found in the LTLO phase [39].

To gain a better understanding of the above observations, we proceed to extract the order parameter assuming that it can be represented by a distortion of B_{1g} symmetry of the high temperature state which induces an anisotropy along the $a = b$ direction. The optical anisotropy can therefore be expressed as,

$$r = \begin{pmatrix} r_a & 0 \\ 0 & r_b \end{pmatrix} + d(T) \begin{pmatrix} 0 & 1 \\ 1 & 0 \end{pmatrix}, \quad (1)$$

where $r_{a/b}$ are the reflectivity coefficients for the electric field polarized along the a/b axis of the *Bmcb* phase and $d(T)$ is the temperature-dependent symmetry-breaking order parameter. In principle, all parameters are complex and $r_{a/b}$ may also be temperature dependent. Using this model, we fit our data to extract a quantity that is proportional to $d^2(T)$ and find that the $r_{a/b}$ coefficients are independent of temperature to within our signal-to-noise, see Appendix A for details.

Figure 2c displays the temperature dependence of d^2 . It can be seen that there is finite symmetry-breaking above T_{COO} , which is approximately two orders of magnitude weaker than when the system crosses into the charge/orbital ordered phase. This observation points to the persistence of some local short-range order (e.g. small COO domains or polarons [40]) well above T_{COO} .

The rotation of the optical axis during the phase transition is particularly interesting. Previous studies of optical anisotropy of layered manganites have only measured fixed directions (parallel and perpendicular with respect to the *Bmcb* phase crystallographic axes) and thus, could not separate contributions from the rotations from decreasing orbital order [41, 42]. Our approach allows us to uncover a sizable rotation. The optical axis should lie along the high symmetry direction in the crystal. For the currently suggested crystal structures, this is along the b_0 axis in both the *Pnma* and *Bmcb* phases. As a result, the onset of charge/orbital ordering should not induce a rotation in the optical axis. Instead, we observe an effect that is consistent with a symmetry breaking at 45 degrees to this axis.

While strain could add an additional symmetry breaking along an arbitrary direction, it seems unlikely that any strain generated during the orbital ordering transition would be larger than the pre-existing strain in the *Bmcb* phase. As there is some ambiguity about the assignment of the *Pnma* [29], we suggest that an alternative space group may be needed for the low tempera-

ture state. Optical spectroscopies can be very sensitive to symmetry breaking, and can respond to small oxygen displacements which may be missed in diffraction. While the issue of the space group could be addressed in future studies, the observation of local order will have implications for the ensuing discussion on the ultrafast dynamics of PCMO.

B. Ultrafast perturbative response

Next, we study the non-equilibrium response of PCMO after being subjected to weak optical excitation at 2.5 mJ/cm^2 in order to characterize the linear response of each phase with a high time resolution and gain insight into the structural response through the coherent phonon spectra and the unoccupied electronic states. Figure 3 shows typical transients measured by our setup. Panel (a) depicts the broadband response measured at 20 K showing ultrafast suppression in transient reflectivity that is additionally modulated by fast oscillations across all probe wavelengths. To analyze the temperature-dependent data, we first perform a principal component analysis (PCA) that decomposes each dataset into a set of significant principal components that capture the variance in signal as a function of wavelength and time. While more than one component is needed to fully describe the transient response [43], we find that the dominant component gives a good representation of the key dynamics in each phase. Figure 3b displays the temporal response derived from the dominant component obtained through the PCA analysis. The electronic response primarily exhibits a decrease in reflectivity followed by a partial recovery across all measured temperatures. In addition, the signal is characterized by the presence of both fast and slow oscillations that vary in amplitude in the different phases. We return to analysis of the temperature-dependent oscillatory response in the next section.

The spectral response also shows a significant temperature dependence (Fig. 3c). At low temperatures, the magnitude of the change is strongest at shorter wavelengths, and the entire measured window shows a reduction in reflectivity. The change is roughly temperature-independent on heating up to T^* , at which point the changes at shorter wavelengths are suppressed, and the dominant response now appears at longer wavelengths. This shift in spectral weight continues until T_{COO} , after which the changes become more or less temperature-independent at long wavelengths, and a small positive signal becomes apparent at shorter wavelengths. To more clearly show this redistribution of spectral weight, Fig. 4 illustrates how the change in reflectivity at the bluest (625 nm) and the reddest (750 nm) measured wavelengths evolves against temperature, revealing opposite trends: the 622 nm signal increases upon heating, while the 750 nm signal decreases. Computing the derivative of $Y = \Delta R_{750 \text{ nm}} - \Delta R_{622 \text{ nm}}$ with respect to tempera-

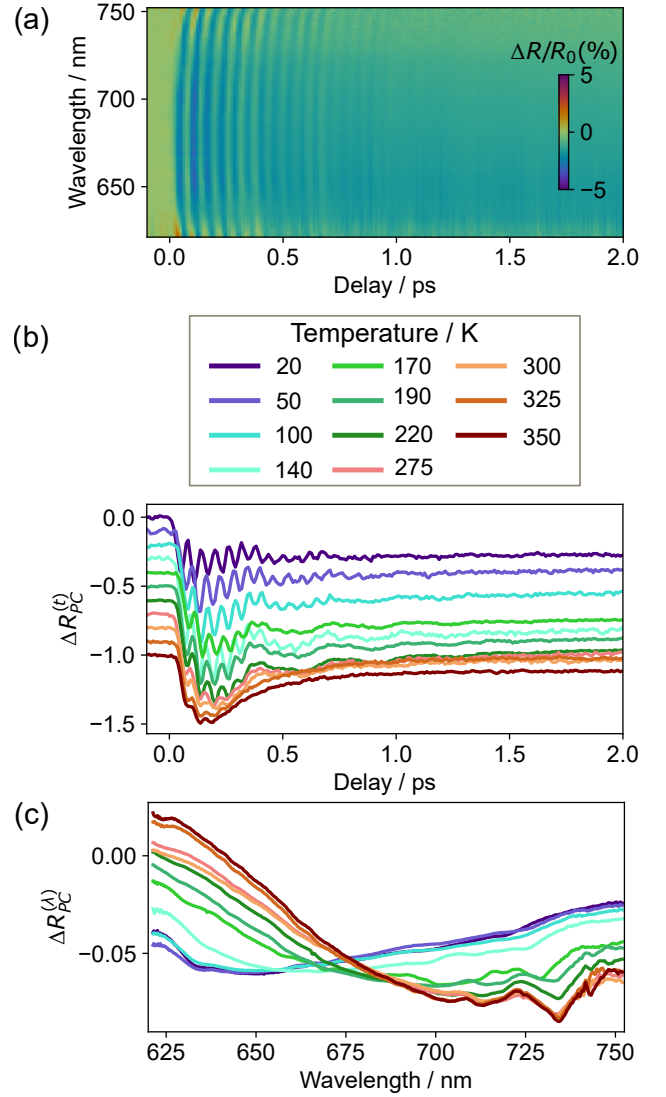


FIG. 3. Transient dynamics of the broadband reflectivity at 2.5 mJ cm^{-2} . (a) Typical broadband change in reflectivity measured at 20 K showing negative change with oscillations due to coherent phonons modulating the transient signal. (b) Temporal dynamics of the dominant principal component obtained from the two-dimensional reflectivity data set for all measured temperatures. (c) Corresponding spectral dependence extracted from the PCA analysis.

ture T , as shown in the inset of Fig. 4, highlights that the largest change in slope with a sign reversal occurs at T^* . This indicates not only that the reflectivity change is strongly wavelength-dependent, but also that it undergoes a notable change of slope at T^* , in contrast to the optical birefringence.

The sensitivity of the differential reflectivity at T^* , instead of T_N , suggests an electronic or structural origin for the change rather than magnetic effects[44]. It is helpful to discuss the wavelength-dependence in the context of electronic structure changes. The optical conductivity (σ_1) of PCMO was previously measured by Majidi *et al.*

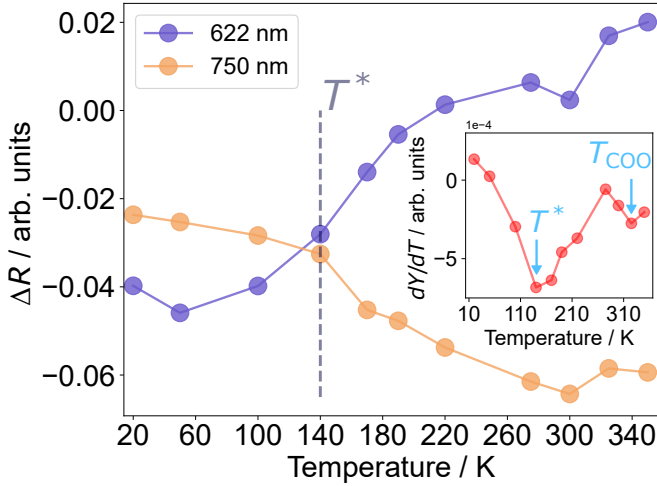


FIG. 4. Temperature-dependent transient reflectivity changes at selected colors representing the two extremes of our detection. The change is strongest at T^* . The inset shows the derivative of Y , which is the difference in the change of reflectivity between 750 and 622 nm, with respect to temperature T . The slope exhibits the largest sign change at T^* .

using spectroscopic ellipsometry, covering the photon energy range from 0.5 to 2.5 eV assigned to charge ordering, and another one at higher photon energies between 2.5 and 4 eV attributed to charge transfer [42]. The charge order peak at 0.8 eV was found to blue shift below T_{COO} as a function of temperature which was attributed to the imbalanced local charges.

In our measurements, the probe covers the energy range of 1.65 – 2 eV, and therefore, we are sensitive to the evolution of electronic states in the charge-ordered region. At low temperatures, photons at higher energies show more pronounced changes than those at lower energies, which can be linked to the optical matrix element effects: higher-energy photons are more easily able to access higher lying states than lower energy ones. Similarly, the spectral transfer of weight as the system is heated could be related to this effect. This demonstrates that the light-matter interaction in PCMO is deeply tied to the evolution of the electronic structure.

C. Coherent phonon dynamics

We now turn our attention to the coherent dynamics that are imprinted in the temporal response. To isolate the phonon contribution from the non-oscillatory dynamics, we undertake fitting of the dominant components shown in Fig. 3b with exponential functions, and subtract the electronic background from raw traces. The residuals are then Fourier-transformed to obtain power spectra at each temperature.

Figure 5 provides an overview of the temperature dependence of the coherent phonon signal when pumped with 2.5 mJ cm^{-2} . Four distinct modes are well-resolved

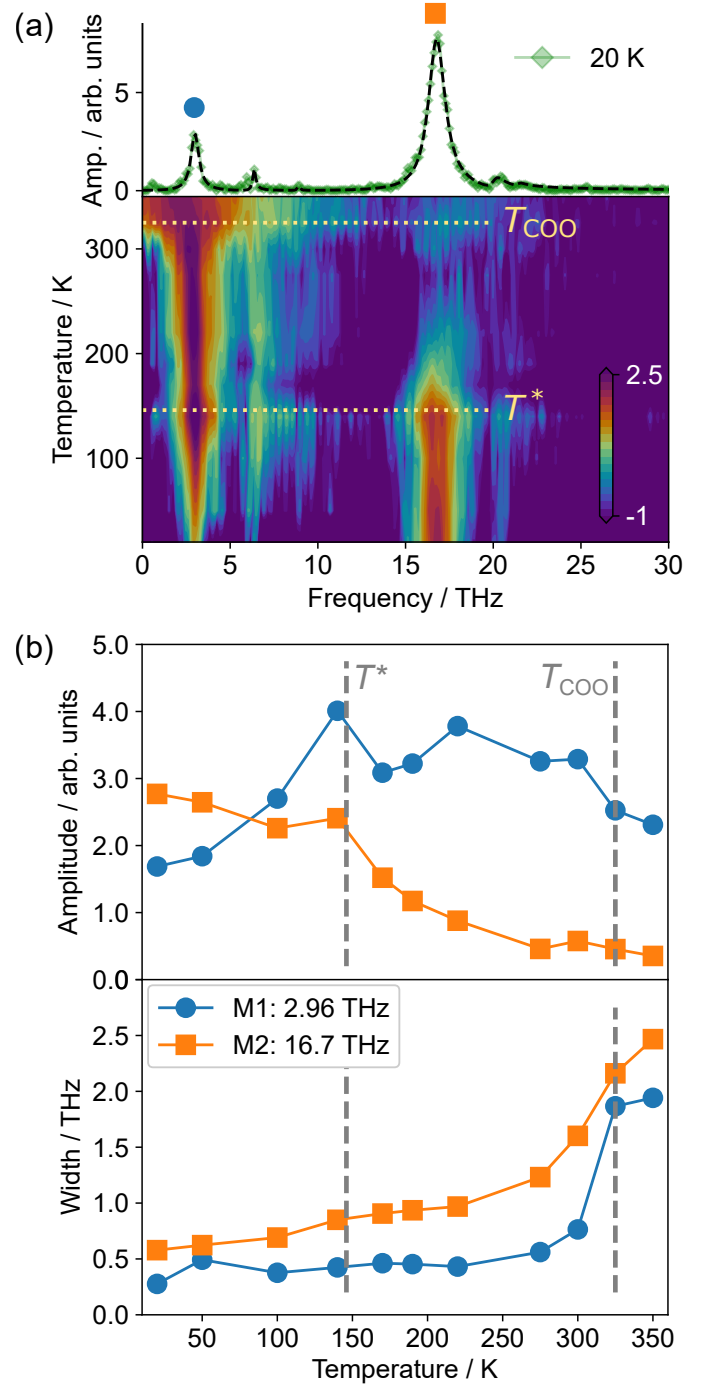


FIG. 5. Coherent phonon response as a function of temperature. (a) Upper panel: Phonon spectrum at 20 K. Dashed line is fit of the spectrum using a multi-Lorentzian oscillator model. Lower panel: Temperature-dependent 2D Fourier map plotted on a log scale showing four phonon modes of which two are examined as labeled by square and circle markers in the upper panel. The yellow horizontal lines denote critical temperatures, T^* and T_{COO} . The color bar provides the amplitude of the modes. (b) Amplitude of the two selected modes against temperature (upper panel) and their widths (lower panel).

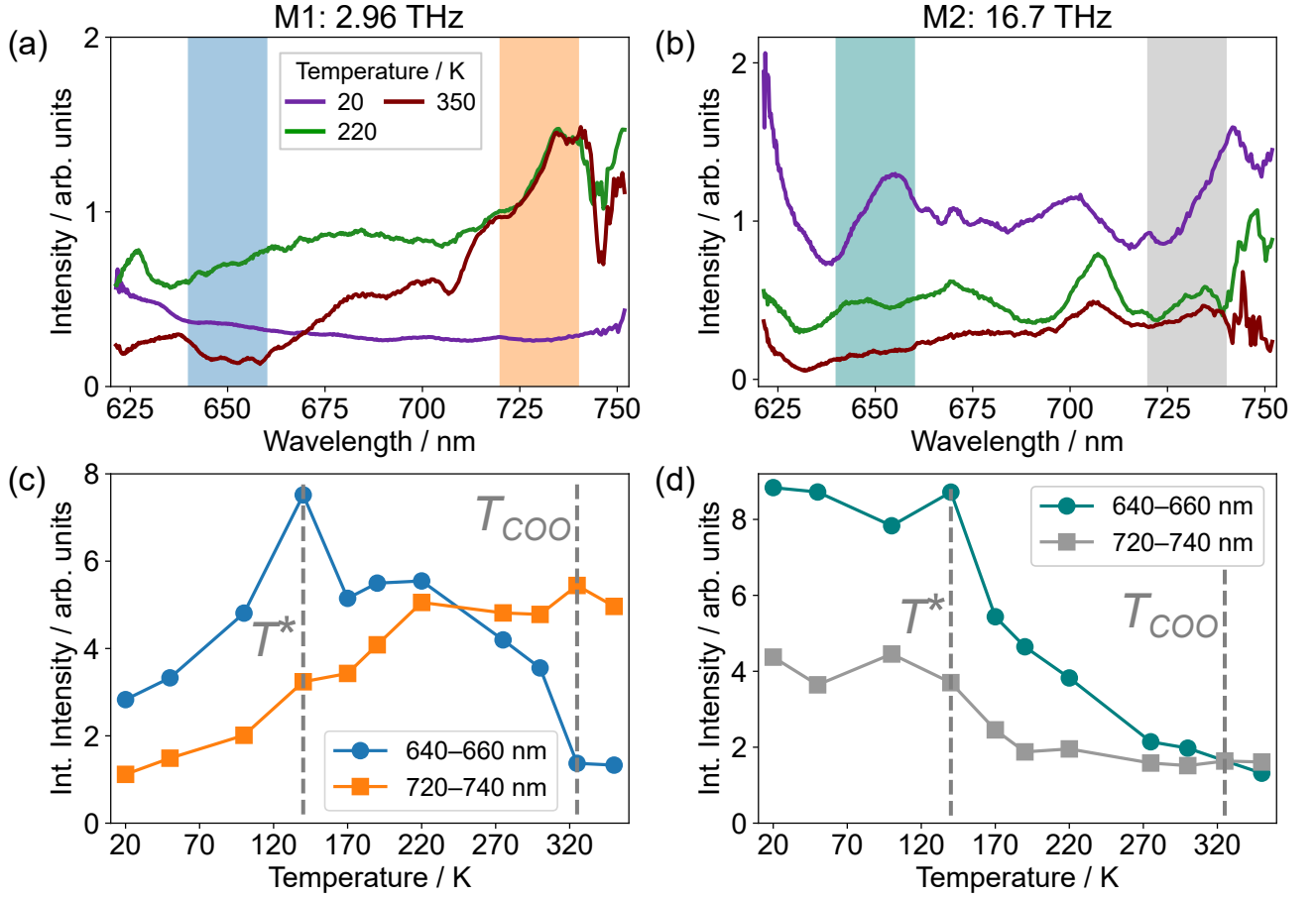


FIG. 6. Temperature and wavelength-dependent amplitude of phonon modes (a) M1 and (b) M2. Shaded regions indicate the spectral ranges used for integration. (c/d) Integrated intensities of the FFT signal for the M1/M2 modes over the two shaded regions indicated in (a/b). The vertical dashed line mark the T^* and T_{COO} transitions.

at 2.96, 6.4, 16.7 and 20.1 THz (99, 213, 557 and 670 cm^{-1}). With the exception of the low frequency, 2.96 THz mode, all others were observed in a previous equilibrium Raman measurements [45] which attests to the sensitivity of detecting phonon modes in our experiment. These four modes also appeared in pump-probe measurements of a related compound LSMO [23], but all modes are systematically higher in frequency in the PCMO compound. The lowest frequency mode shows the strongest shift, increasing by almost 10% from 2.7 THz in LSMO. This is consistent with this mode being assigned to the A-site ionic motion, which are almost a factor of two lighter in PCMO [46]. All modes can be observed in all three phases to varying degrees, but become highly damped above T_{COO} . From a symmetry perspective, these modes should vanish above T_{COO} , but their presence can be attributed to the small fraction of localized, symmetry-broken regions persisting well into the LTO phase, in line with the observations made with optical anisotropy measurements in Fig. 2c.

In the following, we focus on the two most prominent modes: the low-frequency 2.96 THz mode (M1) and the high-frequency 16.7 THz mode (M2), extracting their

widths and amplitudes by simultaneously fitting all peaks at each temperature using a multi-Lorentzian oscillator model (see Fig. 5a, upper panel for a representative fit at 20 K). The M2 mode, previously attributed to the Jahn-Teller distortion of the MnO_6 octahedra, has the highest amplitude at low temperatures (Fig. 5b, upper panel). On heating, the amplitude of this mode slowly decreases until T^* , at which point the rate of change increases, similar to what is observed in the non-oscillatory dynamics shown in Fig. 4, and the amplitude plateaus close to T_{COO} , in good agreement with Raman scattering [45]. The damping rate, which is proportional to the phonon peak width shown in lower panel of Fig. 5b, displays only a moderate increase at T^* , but then a strong increase at T_{COO} . Unlike the cubic compound [33], no significant change in damping due to magnetic ordering is observed, suggesting magneto-elastic coupling is not as strong in the doped single-layered compound, consistent with the reduced colossal magnetoresistance effect in the layered compounds.

The temperature dependence of the M1 peak is more unusual. The intensity now grows on heating up to T^* where it becomes temperature independent until T_{COO} ,

after which it begins to fall. In contrast to the M2 mode, the damping rate of the M1 mode is almost temperature independent up to T_{COO} . Above this temperature, there is a significant broadening and hence, a strong increase in the damping rate.

To better understand the unusual and distinct amplitude response of the M1 mode compared to M2, we examine how the phonon amplitudes vary with the probe wavelength. Figures 6(a, b) show the wavelength-dependent FFT amplitudes of M1 and M2, respectively, at three different temperatures. The shaded regions indicate the spectral ranges used for integration to assess the relative sensitivity at short and long wavelengths as a function of temperature. The resulting integrated signals are plotted in Figs. 6(c, d) for all measured temperatures.

At 20 K, the M1 mode is relatively independent of wavelength, with a slightly greater sensitivity at shorter wavelengths. Similarly, while the M2 mode shows more structure, there is no significant trend with wavelength. However, at higher temperatures, the spectral sensitivity changes significantly. The M1 mode, in particular, becomes significantly stronger at longer wavelengths as the sample is heated, but becomes less sensitive at shorter wavelengths. Consequently, the M1 phonon amplitude is seen to increase up to T^* and is nearly completely suppressed above T_{COO} when measured at 650 nm. In contrast, at 730 nm, it exhibits only a partial suppression above T_{COO} . The M2 mode, on the other hand, is less sensitive to the wavelength and both regions show similar trends. From this data, it is clear that there is no longer a one-to-one correspondence between the physical amplitude of the phonon signal and the measured change in reflectivity.

The trends observed in Figs. 5 and 6 for the M1 mode, namely a pronounced amplitude anomaly at T^* without a corresponding change in the dephasing rate, suggest that the sensitivity of this mode is likely not driven by a change in electron-phonon coupling. Instead, it is linked to the temperature-dependent changes in the electronic states that modulate the light-matter interaction. This observation is further supported by the evolution of the non-oscillatory signal with temperature.

D. Strong excitation below T^*

The observed variations in the phonon amplitude with wavelength raise an interesting question, namely, how can they be connected to structural changes? Typically, the amplitude of the phonon response is taken as a direct measure of the amplitude of the actual atomic displacements. However, as shown above, the fact that the phonon amplitude exhibits a strong wavelength dependence as a function of temperature, even in the relatively low-fluence regime, casts doubts about the validity of this assumption, especially in our case. To test the possible implications of this, we perform a fluence dependence of the signal at 20 K.

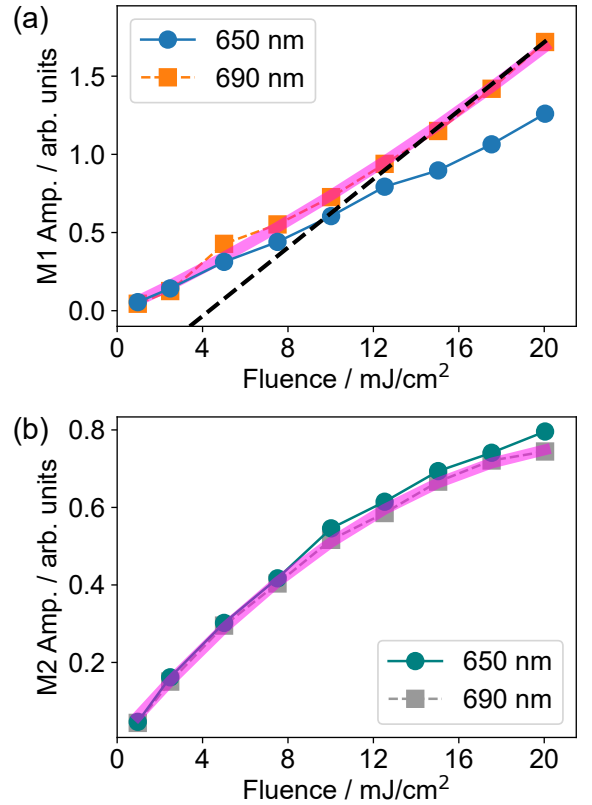


FIG. 7. Fluence dependence of the (a) M1 mode and (b) M2 mode at two distinct wavelengths of 650 nm and 690 nm at 20 K. While M2 mode shows a sublinear behavior leading to saturation at higher fluences for both wavelengths, the M1 mode amplitude exhibits different scaling depending on the wavelength. The thick pink lines are obtained by applying a polynomial function, $Ax + Bx^2$, and serve as a guide-to-the-eye. The black dashed line in (a) cuts the x-axis at around 3.8 mJ cm^{-2} , but is an artifact of the complex wavelength dependence.

In Fig. 7, we plot the fluence dependence of the M1 and M2 phonon mode amplitudes, at two different spectral regions centered at 650 nm and 690 nm, respectively. As can be seen, the M2 mode exhibits sub-linear scaling with fluence independent of the probe wavelength (notice the concave shape of the dependence in Fig. 7b). This behavior is consistent with the idea that increasing fluence applies a stronger driving force on the phonon, while simultaneously acting to suppress the phonon amplitude by action of raising the lattice temperature via electron-phonon thermalization.

The M1 mode, on the other hand, shows a strong wavelength dependence (Fig. 7a). At 650 nm the scaling is linear with fluence, but changing the detection frequency by just 40 nm results in a super-linear behavior at 690 nm. When extrapolating the high fluence data with a linear fit, we find a threshold-like response, denoted by the black dashed line, similar to what was observed in LSMO [34] for the Jahn-Teller mode. In that work, this was interpreted as a signature of a

threshold energy required for melting of orbital-ordered phase, indicating a minimum photodoping concentration was required to release the lattice motion, thus assigning a structural origin for stabilizing the orbitally-ordered state in LSMO. However, such an effect was not seen in later work which probed at a different wavelength [23]. In the present work, the nonlinearity is observed in the M1 mode, which involves the motion of the A-site ions, and does not directly mediate the COO phase through the Jahn-Teller distortions. On the other hand, a linear response can be obtained if the appropriate wavelength is examined. Taken together with low-fluence and wavelength-resolved data, these observations suggest that the apparent threshold behavior is an artifact that arises due to the breakdown in linear coupling between phonon amplitude and detection rather than a true physical threshold.

We note that the wavelength response of the M1 mode (Fig. 6a) shows very similar changes as the electronic background (Fig. 3c), with both showing an increase in sensitivity at longer wavelengths at higher temperatures. This indicates that the same electronic states populated or depopulated by the pump are also modulated by the M1 phonon. This could give rise to an enhanced nonlinearity arising from a cross term between the electronic and phonon contribution to the reflectivity change of the form,

$$dR_Q(\lambda, t) = \left(\frac{dR}{dQ}(\lambda) + \frac{d^2R}{dQdn_e}(\lambda)n_e(t) \right) Q(t), \quad (2)$$

where $dR_Q(\lambda, t)$ is the reflectivity change as a function of the probe wavelength due to the phonon Q , and n_e is the photoinduced change in the carriers. As both Q and n_e depend linearly on the pump intensity for low intensities, a nonlinear fluence dependence will arise at probe wavelengths where $\frac{d^2R}{dQdn_e}(\lambda)$ is large. We note that $n_e(t)$ is a relatively slowly changing function of time after the initial rise, and will unlikely impact that phonon line shape significantly.

IV. CONCLUSIONS

In summary, our combined optical birefringence and ultrafast spectroscopy experiments reveal new insights into the complex phase diagram of PCMO. Upon entering the COO phase, the optical axis undergoes a pronounced rotation, indicative of a phase with potentially lower symmetry than the currently proposed $Pnma$. Moreover, evidence of local short-range order of the COO phase was observed above T_{COO} which enables the appearance of Raman-active phonons associated with COO above the phase transition temperature.

Among the phonon modes, the 2.96 THz mode, linked to A-site ionic motions, exhibits a strong wavelength and temperature-dependence, including displaying sub- and superlinear scaling with fluence depending on the probe

wavelengths, reflecting a breakdown in the linear relationship between the amplitude of the detected phonon-induced change in reflectivity and the actual phonon amplitude. To this end, our broadband measurements further emphasize how artifacts can arise, leading to misinterpretations of the electronic response when probing at a single wavelength.

Finally, the complex behaviors uncovered here, stemming from rich light-matter interactions, distinguish PCMO from other layered manganites like LSMO, making it more susceptible to external stimuli and highly amenable to photoengineering thereby offering a platform to explore new, possibly hidden, phases.

ACKNOWLEDGMENTS

We thank Urs Staub for insightful comments on the structure of $\text{Pr}_{0.5}\text{Ca}_{1.5}\text{MnO}_4$. We acknowledge funding from the Novo Nordisk Foundation (NNF23OC0084990) and support from the Center for Integrated Materials Research (iMAT) at Aarhus University. A.S.J. acknowledges the support of the Ramón y Cajal Program (Grant No. RYC2021-032392-I). IMDEA Nanociencia acknowledges support from the “Severo Ochoa” Programme for Centers of Excellence in R&D (MICIN, CEX2020-001039-S).

DATA AVAILABILITY STATEMENT

All data used in this manuscript is available from a Zenodo repository [38].

Appendix A

In this section, we discuss how the order parameter can be extracted from the birefringent signal. The reflectivity in the Bmb orthorhombic phase can be expressed as

$$r_0 = \begin{pmatrix} a & 0 & 0 \\ 0 & b & 0 \\ 0 & 0 & c \end{pmatrix} \quad (\text{A.1})$$

We assume that the order parameter can be expressed as a B_g mode which induces an anisotropy in the ab plane as

$$\eta = \begin{pmatrix} 0 & d & 0 \\ d & 0 & 0 \\ 0 & 0 & 0 \end{pmatrix}, \quad (\text{A.2})$$

where d is a function of temperature. We note that A_{1g} modes will not result in a change of optical axis, and thus have been neglected here.

This gives the temperature-dependent reflectivity as

$$r(T) = r_0 + \eta(T) = \begin{pmatrix} a & d & 0 \\ d & b & 0 \\ 0 & 0 & c \end{pmatrix} \quad (\text{A.3})$$

The probe light is polarized in the ab -plane, making an angle θ to the a -axis defined as

$$E_i = E_0 = \begin{pmatrix} \cos \theta \\ \sin \theta \\ 0 \end{pmatrix} \quad (\text{A.4})$$

In the experimental setup, as described in [36], the polarization component parallel to the incident light is detected this gives,

$$E(\theta) = \frac{1}{E_0} E_i^T r E_i = E_0 \left(\alpha_+ + \sqrt{\alpha_-^2 + d^2} \cos(2\theta - \phi) \right), \quad (\text{A.5})$$

Where

$$\alpha_{\pm} = \frac{a \pm b}{2}, \quad (\text{A.6})$$

and

$$\cos \phi = \frac{\alpha_-}{\sqrt{\alpha_-^2 + d^2}}. \quad (\text{A.7})$$

In principle, each coefficient can be complex. The detected intensity can then be written as,

$$I(\theta)/I_0 = I_{DC} + I_2 \cos(2\theta + \phi_2) + I_4 \cos(4\theta + \phi_4). \quad (\text{A.8})$$

Where $I_0 = E_0^2$,

$$I_2 = 2\alpha_{+-} \sqrt{1 + \frac{d_+^2}{\alpha_{+-}^2}} = \frac{\alpha_{+-}}{\cos \phi}, \quad (\text{A.9})$$

$$\alpha_{+-} = \Re\{\alpha_+ \alpha_-^*\}, \quad (\text{A.10})$$

and

$$d_+ = \Re\{\alpha_+ d^*\}, \quad (\text{A.11})$$

Equation A.8 is fitted to the experimental data shown in Fig.2a, giving I_2 and ϕ_2 . These can then be used to obtain d_+ as a function of temperature, as shown in Fig.2c.

-
- [1] E. Dagotto, *Science* **309**, 257 (2005).
 - [2] E. H. da Silva Neto, P. Aynajian, A. Frano, R. Comin, E. Schierle, E. Weschke, A. Gyenis, J. Wen, J. Schneeloch, Z. Xu, S. Ono, G. Gu, M. Le Tacon, and A. Yazdani, *Science* **343**, 393 (2014).
 - [3] Y. Tokura, M. Kawasaki, and N. Nagaosa, *Nature Physics* **13**, 1056 (2017).
 - [4] J. F. Mitchell, C. D. Ling, J. E. Millburn, D. N. Argyriou, A. Berger, and M. Medarde, *Journal of Applied Physics* **89**, 6618 (2001).
 - [5] Y. Tomioka, X. Z. Yu, T. Ito, Y. Matsui, and Y. Tokura, *Physical Review B* **80**, 094406 (2009).
 - [6] S. Jin, T. H. Tiefel, M. McCormack, R. A. Fastnacht, R. Ramesh, and L. H. Chen, *Science* **264**, 413 (1994).
 - [7] E. Dagotto, T. Hotta, and A. Moreo, *Physics Reports* **344**, 1 (2001).
 - [8] K.-i. Chahara, T. Ohno, M. Kasai, and Y. Kozono, *Applied Physics Letters* **63**, 1990 (1993).
 - [9] M. Fiebig, K. Miyano, Y. Tomioka, and Y. Tokura, *Science* **280**, 1925 (1998).
 - [10] D. Polli, M. Rini, S. Wall, R. W. Schoenlein, Y. Tomioka, Y. Tokura, G. Cerullo, and A. Cavalleri, *Nature materials* **6**, 643 (2007).
 - [11] M. Rini, R. Tobey, N. Dean, J. Itatani, Y. Tomioka, Y. Tokura, R. W. Schoenlein, and A. Cavalleri, *Nature* **449**, 72 (2007).
 - [12] M. Rini, Y. Zhu, S. Wall, R. Tobey, H. P. Ehrke, T. Garl, J. Freeland, Y. Tomioka, Y. Tokura, A. Cavalleri, and R. Schoenlein, *Physical Review B* **80**, 155113 (2009).
 - [13] T. Li, A. Patz, L. Mouchliadis, J. Yan, T. A. Lograsso, I. E. Perakis, and J. Wang, *Nature* **496**, 69 (2013).
 - [14] S. Wall, M. Rini, S. S. Dhesi, R. W. Schoenlein, and A. Cavalleri, *IEEE Journal of Selected Topics in Quantum Electronics* **18**, 81 (2012).
 - [15] H. Ichikawa, S. Nozawa, T. Sato, A. Tomita, K. Ichiyangi, M. Chollet, L. Guerin, N. Dean, A. Cavalleri, S.-i. Adachi, T.-h. Arima, H. Sawa, Y. Ogimoto, M. Nakamura, R. Tamaki, K. Miyano, and S.-y. Koshihara, *Nature Materials* **10**, 101 (2011).
 - [16] M. Tokunaga, N. Miura, Y. Moritomo, and Y. Tokura, *Physical Review B* **59**, 11151 (1999).
 - [17] S. S. Dhesi, A. Mirone, C. De Nadaï, P. Ohresser, P. Benck, N. B. Brookes, P. Reutler, A. Revcolevschi, A. Tagliaferri, O. Toulemonde, and G. van der Laan, *Physical Review Letters* **92**, 056403 (2004).
 - [18] S. B. Wilkins, P. D. Spencer, P. D. Hatton, S. P. Collins, M. D. Roper, D. Prabhakaran, and A. T. Boothroyd, *Physical Review Letters* **91**, 167205 (2003).
 - [19] C. W. M. Castleton and M. Altarelli, *Physical Review B* **62**, 1033 (2000).
 - [20] T. Ogasawara, T. Kimura, T. Ishikawa, M. Kuwata-Gonokami, and Y. Tokura, *Physical Review B* **63**, 113105 (2001).
 - [21] H. Ehrke, R. I. Tobey, S. Wall, S. A. Cavill, M. Först, V. Khanna, T. Garl, N. Stojanovic, D. Prabhakaran, A. T. Boothroyd, M. Gensch, A. Mirone, P. Reutler, A. Revcolevschi, S. S. Dhesi, and A. Cavalleri, *Physical Review Letters* **106**, 217401 (2011).

- [22] R. I. Tobey, S. Wall, M. Först, H. Bromberger, V. Khanna, J. J. Turner, W. Schlotter, M. Trigo, O. Krupin, W. S. Lee, Y. D. Chuang, R. Moore, A. L. Cavalieri, S. B. Wilkins, H. Zheng, J. F. Mitchell, S. S. Dhesi, A. Cavalleri, and J. P. Hill, *Physical Review B* **86**, 064425 (2012).
- [23] D. Perez-Salinas, A. S. Johnson, D. Prabhakaran, and S. Wall, *Nature Communications* **13**, 238 (2022).
- [24] M. Monti, K. M. Siddiqui, D. Perez-Salinas, N. Agarwal, M. Bremholm, X. Li, D. Prabhakaran, X. Liu, D. Babich, M. Sander, Y. Deng, H. T. Lemke, R. Mankowsky, X. Liu, and S. E. Wall, *arXiv:2407.03013* (2024), *arXiv:2407.03013*.
- [25] R. I. Tobey, D. Prabhakaran, A. T. Boothroyd, and A. Cavalleri, *Physical Review Letters* **101**, 197404 (2008).
- [26] M. Först, R. I. Tobey, S. Wall, H. Bromberger, V. Khanna, A. L. Cavalieri, Y. D. Chuang, W. S. Lee, R. Moore, W. F. Schlotter, J. J. Turner, O. Krupin, M. Trigo, H. Zheng, J. F. Mitchell, S. S. Dhesi, J. P. Hill, and A. Cavalleri, *Physical Review B* **84**, 241104 (2011).
- [27] T. A. Miller, R. W. Chhajlany, L. Tagliacozzo, B. Green, S. Kovalev, D. Prabhakaran, M. Lewenstein, M. Gensch, and S. Wall, *Nature Communications* **6** (2015).
- [28] X. Z. Yu, R. Mathieu, T. Arima, Y. Kaneko, J. P. He, M. Uchida, T. Asaka, T. Nagai, K. Kimoto, A. Asamitsu, Y. Matsui, and Y. Tokura, *Physical Review B* **75**, 174441 (2007).
- [29] O. J. Schumann, *Structural Investigations on layered Manganites and Ruthenates*, PhD Thesis, University of Cologne (2010).
- [30] M. Porer, L. Rettig, E. M. Bothschafter, V. Esposito, R. B. Versteeg, P. H. Van Loosdrecht, M. Savoini, J. Rittmann, M. Kubli, G. Lantz, O. J. Schumann, A. A. Nugroho, M. Braden, G. Ingold, S. L. Johnson, P. Beaud, and U. Staub, *Physical Review B* **101**, 75119 (2020).
- [31] V. Capogrosso, *Dimensionality and ordering effects on the electronic structure of low dimensional strongly correlated electron transition metal oxides*, PhD Thesis, Università degli Studi di Trieste (2011).
- [32] S. Chi, F. Ye, P. Dai, J. A. Fernandez-Baca, Q. Huang, J. W. Lynn, E. W. Plummer, R. Mathieu, Y. Kaneko, and Y. Tokura, *Proceedings of the National Academy of Sciences* **104**, 10796 (2007).
- [33] S. Wall, D. Prabhakaran, A. Boothroyd, and A. Cavalleri, *Physical Review Letters* **103**, 097402 (2009).
- [34] R. Singla, A. Simoncig, M. Först, D. Prabhakaran, A. L. Cavalieri, and A. Cavalleri, *Physical Review B* **88**, 075107 (2013).
- [35] H. Matsuzaki, H. Uemura, M. Matsubara, T. Kimura, Y. Tokura, and H. Okamoto, *Physical Review B* **79**, 235131 (2009).
- [36] K. M. Siddiqui, H. Strojcka, T. H. Meyland, N. Khatiwada, N. Klinkby, D. Perez-Salinas, and S. E. Wall, A versatile setup for symmetry-resolved ultrafast dynamics of quantum materials (2025), 2505.04855 [cond-mat].
- [37] E. B. Amuah, A. S. Johnson, and S. E. Wall, *Review of Scientific Instruments* **92**, 103003 (2021).
- [38] E. B. Amuah, K. Siddiqui, and M. Monti, Broadband time-resolved reflectivity data on $\text{Pr}_{0.5}\text{Ca}_{1.5}\text{MnO}_4$ as a function of temperature and fluence (2025).
- [39] C. Flathmann, T. Meyer, U. Ross, A. Dehning, C. Jooss, and M. Seibt, *APL Materials* **12**, 061112 (2024).
- [40] D. B. Romero, V. B. Podobedov, A. Weber, J. P. Rice, J. F. Mitchell, R. P. Sharma, and H. D. Drew, *Physical Review B* **58**, R14737 (1998).
- [41] Y. S. Lee, S. Onoda, T. Arima, Y. Tokunaga, J. P. He, Y. Kaneko, N. Nagaosa, and Y. Tokura, *Physical Review Letters* **97**, 077203 (2006).
- [42] M. A. Majidi, E. Thoeng, P. K. Gogoi, F. Wendt, S. H. Wang, I. Santoso, T. C. Asmara, I. P. Handayani, P. H. M. van Loosdrecht, A. A. Nugroho, M. Rübhausen, and A. Rusydi, *Physical Review B* **87**, 235135 (2013).
- [43] E. B. Amuah, K. M. Siddiqui, M. Monti, A. S. Johnson, and S. E. Wall, *Optics Express* **32**, 3817 (2024).
- [44] E. Pastor, D. Moreno-Mencía, M. Monti, A. S. Johnson, N. Fleischmann, C. Wang, Y. Shi, X. Liu, D. G. Mazzone, M. P. M. Dean, and S. Wall, *Physical Review B* **105**, 064409 (2022).
- [45] I. P. Handayani, A. A. Nugroho, S. Riyadi, G. R. Blake, N. Mufti, T. T. M. Palstra, and P. H. M. van Loosdrecht, *Physical Review B* **92**, 205101 (2015).
- [46] V. A. Amelichev, B. Güttler, O. Yu. Gorbenko, A. R. Kaul, A. A. Bosak, and A. Yu. Ganin, *Physical Review B* **63**, 104430 (2001).